5

Terahertz Radiation from Carbon Nanotubes

A. M. Nemilentsau
Belarus State University

G. Ya. Slepyan
Belarus State University

S. A. Maksimenko
Belarus State University

O. V. Kibis
Novosibirsk State Technical University

M. E. Portnoi
University of Exeter

5.1 Introduction

Creating a compact, reliable source of terahertz (THz) radiation is one of the most challenging problems in contemporary applied physics (Lee and Wanke, 2007). Despite the fact that THz technology is at the boundaries of microwave and photonic technologies, it is quite underdeveloped compared to the achievements in the microwave or the photonic technology. There are very few commercially available instruments for the THz frequency region, and most of them lack the precision required to perform accurate measurements. There are also no miniaturized and low-cost THz sources. One of the latest trends in THz technology (Dragoman and Dragoman, 2004a) is to use single-walled carbon nanotubes (SWNTs) as building blocks of novel high-frequency devices.

An SWNT is a hollow cylindrical molecule made up of carbon atoms (Saito et al., 1998). We can formally consider the SWNT as a graphene sheet rolled up into a cylinder along the vector $\mathbf{R}_h$ connecting to crystallographically equivalent sites of the graphene lattice (see Figure 5.1). This vector is called the chiral vector and is usually defined in terms of the basic vectors, $\mathbf{a_1}$ and $\mathbf{a_2}$, of the graphene lattice: $\mathbf{R}_h = m\mathbf{a_1} + n\mathbf{a_2}$, where m, n are integers. The dual index (m, n) is usually used to characterize SWNT type. Three different SWNT types are defined: $(m, 0)$ zigzag SWNTs, (m, m) armchair SWNTs, and (m, n) $(0 < n \neq m)$ chiral SWNTs. The SWNT radius, R_{cn}, and chiral angle, θ (the angle between the $\mathbf{R}_h$ and a_1) are defined as follows:

$$R_{cn} = \frac{|\mathbf{R}_h|}{2\pi} = \frac{\sqrt{3}b}{2\pi}\sqrt{m^2 + mn + n^2}, \tag{5.1}$$

$$\cos\theta = \frac{\mathbf{R}_h \cdot \mathbf{a}_1}{|\mathbf{R}_h||\mathbf{a}_1|} = \frac{2n+m}{2\sqrt{n^2+nm+m^2}}, \tag{5.2}$$

where $b = 0.142\,nm$ is the C–C bond length. Typically, SWNTs are 0.1–$10\,\mu m$ in length; their cross-sectional radius varies within the range 1–$10\,nm$, while their chiral angle is $0 \leq \theta_{cn} \leq 30°$.

There are several promising proposals of using carbon nanotubes for THz applications including a nanoklystron using extremely efficient high-field electron emission from nanotubes (Dragoman and Dragoman, 2004a; Manohara et al., 2005; Di Carlo et al., 2006); devices based on negative differential conductivity (NDC) in large-diameter semiconducting SWNTs (Maksimenko and Slepyan, 2000; Pennington and Goldsman, 2003); high-frequency resonant-tunneling diodes (Dragoman and Dragoman, 2004b) and Schottky diodes (Léonard and Tersoff, 2000; Odintsov, 2000; Yang et al., 2005; Lu et al., 2006); as well as electric-field-controlled carbon nanotube superlattices (Kibis et al., 2005a,b), frequency multipliers (Slepyan et al., 1999, 2001), THz amplifiers (Dragoman and Dragoman, 2005), and switches (Dragoman et al., 2006). Among others, the idea of SWNT-based optical devices enabling the control and enhancement of radiation efficiency on the nanoscale, i.e., nanoscale antennas for THz, infrared, and visible light, is actively
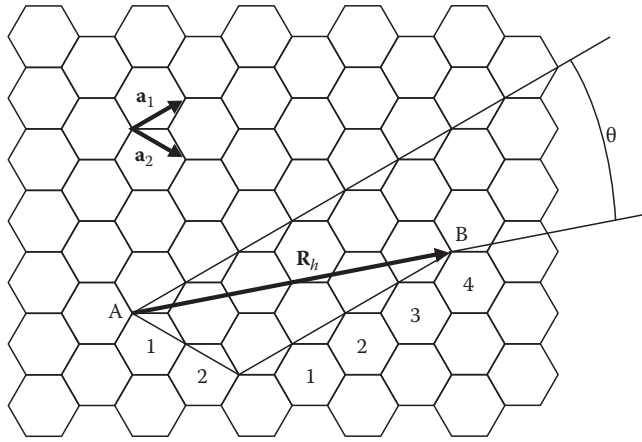
FIGURE 5.1 Graphene crystalline lattice. Each lattice node contains a carbon atom.

discussed (Dresselhaus, 2004; Hanson, 2005; Burke et al., 2006; Slepyan et al., 2006). Noise properties and operational limits of such antennas are substantially determined by the thermal fluctuations of the electromagnetic field.

In this chapter, several novel schemes are discussed (Kibis and Portnoi, 2005; Portnoi et al., 2006; Kibis et al., 2007, 2008; Nemilentsau et al., 2007; Portnoi et al., 2008) to utilize the physical properties of SWNTs for the generation and detection of THz radiation.

5.2 Electronic Properties of SWNTs

Electrodynamic processes in any medium are dictated by its electronic properties, although they may be missing in an explicit form of the macroscopic electrodynamics equations. In that sense, SWNTs are not an exception. Many researches (Charlier et al., 2007) have been devoted to the development of the theory of electronic properties of the SWNT. Both the sophisticated methods of modern solid-state physics and first-principles simulations are among them. In this section, we give only an elementary introduction for later use in the analysis of the THz radiation from SWNTs.

Each carbon atom in graphene and SWNT has four valence orbitals ($2s$, $2p_x$, $2p_y$, and $2p_z$). Three orbitals (s, p_x, and p_y) combine to form in-plane σ orbitals. The σ bonds are strong covalent bonds responsible for most of the binding energy and elastic properties of the graphene sheet and SWNT. The remaining p_z orbital, pointing out of the graphene she et, cannot couple with σ orbitals. The lateral interaction with the neighboring p_z orbitals creates delocalized π orbitals. The π bonds are perpendicular to the surface of the SWNT and are responsible for the weak interaction between SWNTs in a bundle, similar to the weak interaction between graphene layers in pure graphite. The energy levels associated with the in-plane bonds are known to be far away from the Fermi energy in graphene, and thus do not play a key role in its electronic properties. In contrast, the bonding and antibonding π bands cross the Fermi level at high-symmetry

points in the Brillouin zone of graphene (Wallace, 1947). Thus, we restrict our consideration to the π electrons, assuming that their movement can be described in the framework of the tight-binding approximation (Saito et al., 1998); the overlapping of wave functions of only the nearest atoms is taken into account. In the beginning, we apply this approach to the plane monoatomic graphite layer, and then show how the model must be modified to analyze an SWNT.

To describe graphene π bands we use the 2 × 2 Hamiltonian matrix (Wallace, 1947):

$$\hat{\mathbf{H}}_0 = \begin{pmatrix} 0 & H_{12}(p_x, p_y) \\ H_{12}^*(p_x, p_y) & 0 \end{pmatrix}, \qquad (5.3)$$

where

$$H_{12}(p_x, p_y) = -\gamma_1 \exp\left\{i\frac{b}{\hbar}p_x\right\} - \gamma_2 \exp\left\{i\frac{b}{\hbar}\left(\frac{1}{2}p_x - \sqrt{3}p_y\right)\right\}$$

$$-\gamma_3 \exp\left\{-i\frac{b}{\hbar}\left(\frac{1}{2}p_x - \sqrt{3}p_y\right)\right\}. \qquad (5.4)$$

Here, $\gamma_{1,2,3}$ are the overlapping integrals; $p_{x,y}$ are the projections of the quasi momentum of electrons, **p**, on the corresponding axes; and $\hbar$ is the Planck constant. As the electronic properties of graphene are isotropic in the in-plane, we set $\gamma_1 = \gamma_2 = \gamma_3 = \gamma_0$ in Equation 5.4, where $\gamma_0 \simeq 3$ eV is the phenomenological parameter, which can be determined experimentally (see, e.g., Saito et al., 1998). The electron energy values are found as the eigenvalues of the matrix on the right side of (5.3) as

$$\varepsilon_{c,v}(\mathbf{p}) = \pm\gamma_0\sqrt{1 + 4\cos\left(\frac{3bp_x}{2\hbar}\right)\cos\left(\frac{\sqrt{3}bp_y}{2\hbar}\right) + 4\cos^2\left(\frac{\sqrt{3}bp_y}{2\hbar}\right)}. $$

$$(5.5)$$

The plus and minus signs in this equation correspond to conduction (*c*) and valence (υ) bands, respectively. The range of AQ1 definition of the quasi momentum, **p** (the first Brillouin zone), are the hexagons shown in Figure 5.2. The vertices are the Fermi points where ε = 0, which is indicative of the absence of the forbidden zone for π electrons in graphene.

The dispersion properties of electrons in SWNTs are quite different from those in graphene, as a plane monolayer is transformed into a cylinder. In a cylindrical structure, an electron located at the origin and an electron located at the position defined by the vector $\mathbf{R}_h = m\mathbf{a}_1 + n\mathbf{a}_2$ are identical. Hence, we should impose the periodic boundary conditions along the tube circumference on the wave functions of π electrons in SWNTs:

$$\Psi(\mathbf{r} + \mathbf{R}_h) = e^{i\mathbf{p}\mathbf{R}_h/\hbar}\Psi(\mathbf{r}) = \Psi(\mathbf{r}). \qquad (5.6)$$
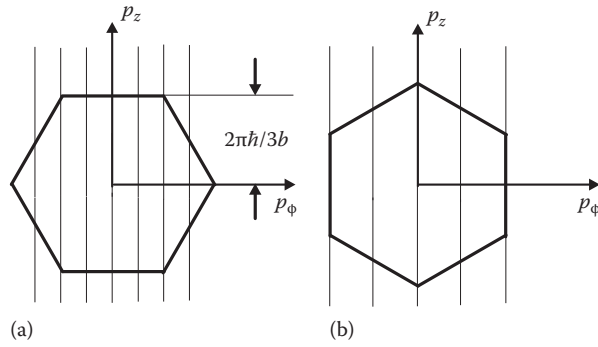
FIGURE 5.2 First Brillouin zone for (a) zigzag and (b) armchair SWNTs.

The second equality here is due to the Bloch theorem. This leads to the quantization of the transverse quasi momentum of electrons:

$$p_\phi = \hbar s / R_{cn}, \qquad (5.7)$$

where s is an integer. The cylindrical coordinate system with the z-axis oriented along the SWNT axis is used here. The axial projection, p_z, of the quasi momentum is continuous. In order to derive the dispersion equation for zigzag SWNTs from Equation 5.5, one must perform the substitutions $\{p_x \to p_z, p_y \to p_\phi\}$, which yields

$$\varepsilon_{c,v}(p_z, s) = \pm \gamma_0 \sqrt{1 + 4\cos\left(\frac{3bp_z}{2\hbar}\right)\cos\left(\frac{\pi s}{m}\right) + 4\cos^2\left(\frac{\pi s}{m}\right)},$$

$$s = 1, 2, \ldots, m. \qquad (5.8)$$

For armchair SWNTs, the dispersion law is obtained from Equation 5.5 by means of the substitutions $\{p_x \to p_\phi, p_y \to p_z\}$. For chiral SWNTs, the analogous procedure is specified by $\{p_x \to p_z \cos\theta + p_\phi \sin\theta, p_x \to p_z \sin\theta - p_\phi \cos\theta\}$.

It follows from Equation 5.7 that the first Brillouin zone in SWNTs is transformed from a hexagon to a family of one-dimensional zones defined by segments of straight lines confined to the interior of the hexagon. Depending on the dual index (m,n), these segments can be oriented differently either by bypassing or crossing the Fermi points, as shown in Figure 5.2. Correspondingly, the forbidden zone either appears or disappears in the electron spectrum of an SWNT. In the absence of the forbidden zone, a material is a metal; otherwise, it is a semiconductor. The condition for the forbidden zone to appear is (Saito et al., 1998)

$$m - n \neq 3q, \qquad (5.9)$$

where q is an integer. For armchair SWNTs, this condition is not valid at any m, and the forbidden zone is always absent, thus proving that the armchair SWNTs are always metallic. For zigzag SWNTs, the zone appears when $m \neq 3q$, and, thus, zigzag SWNTs can be either metallic or semiconducting, depending on R_{cn}.

Strictly speaking, the curvature of the SWNT surface breaks the isotropic symmetry of electronic properties so that the overlapping integrals, $\gamma_{1,2,3}$, in Equation 5.4 turn out to be different from one another. For the zigzag SWNTs, these integrals are as follows (Kane and Mele, 1997; Lin and Chuu, 1998): $\gamma_1 = \gamma_0$, $\gamma_2 = \gamma_3 = (1 - 3b^2/32R_{cn}^2)\gamma_0$. Then, instead of Equation 5.8, we have the dispersion equation:

$$\varepsilon_{c,v}(p_z, s) = \pm \sqrt{\gamma_0^2 + 4\gamma_0\gamma_2\cos\left(\frac{3bp_z}{2\hbar}\right)\cos\left(\frac{\pi s}{m}\right) + 4\gamma_2^2\cos^2\left(\frac{\pi s}{m}\right)},$$

$$(5.10)$$

which shows the presence of the forbidden zone even for $m = 3q$. However, this zone is much narrower compared to that for $m \neq 3q$.

The nontrivial electronic structure of SWNTs dictates their response to the electromagnetic field. Due to the quasi one-dimensional nature of SWNTs, their optical response is strongly anisotropic. The optical response to the axially polarized incident electric field significantly exceeds the optical response to the electric field polarized transversely to the CNT (carbon nanotube) axis (Tasaki et al., 1998; Milošević et al., 2003; Murakami et al., 2005). Due to the quantization of the transverse quasi momentum of electrons (Equation 5.7), divergences arise in the electronic density of states (DOS) of SWNTs (Saito et al., 1998). These divergences, which are known as Van Hove singularities, produce discrete energy levels or "subbands," the energy of which is determined solely by the chirality of SWNTs (Saito et al., 1998). As the inter-subband gap corresponds to the energy of infrared to visible light, the spectra of optical conductivity of an SWNT demonstrate the number of resonant lines in the region.

In the spectral range of 1–100 THz, the nonmonotonic frequency dependence of the reflectance and transmittance of CNT-based composite media that does not follow from the standard Drude theory has been observed (Ugawa et al., 1999; Ruzicka et al., 2000). Ugawa et al. (1999) found empirically that the effective permittivity of a CNT-based composite medium can be represented as a superposition of Drudian and Lorentzian functions. The spectral width of the resonance is of the order of the resonant frequency. The origin of this resonance could be attributed the inhomogeneously broadened geometric resonance in an isolated CNT (Slepyan et al., 2006).

5.3 Thermal Radiation from SWNTs

In this section, we investigate the thermal electromagnetic field radiated by an SWNT at temperature T placed in cold environment and show that the thermal radiation from metallic SWNTs can serve as an efficient source of the THz radiation. Our consideration is based on the method developed by Rytov (1958), which known as fluctuational electrodynamics (see details in Lifshitz and Pitaevskii, 1980; Rytov et al., 1989; Joulain et al., 2005). The key idea of this method is that the thermal radiation sources in

a material are the fluctuation currents, which are due to the random thermal motion of charged carriers the material consists. To determine the statistical properties of the electromagnetic field we have to know the statistical properties of random currents and the radiation of the elemental volume of the material. The first information is given by the fluctuation-dissipative theorem while the second information is given by the Green tensor of the system. It should be noted that the application of the equilibrium laws, such as the fluctuation-dissipative theorem, is not very rigorous in this case, but it is justified when the role of the heat transport phenomena (such as thermal conductivity) is negligible. Hence, we will not consider them further.

The thermal radiation from SWNTs is of interest not only because of possible applications of THz device. Fundamental interest to the thermal radiation is dictated by the ability of nanostructures to change the *photonic local density of states* (LDOS), i.e., the electromagnetic vacuum energy (Agarwal, 1975; Joulain et al., 2003; Novotny and Hecht, 2006). The effect has been observed in microcavities, photonic crystals, and nanoparticles in the vicinity of surface-plasmon resonances (Novotny and Hecht, 2006). Thus, as the electromagnetic fluctuations are defined by photonic LDOS, the investigation of the thermal radiation is expected to bring new opportunities for the reconstruction of photonic LDOS in the presence of nanostructures. The apertureless scanning near-field optical microscopy provides a possibility for the experimental detection of LDOS (Joulain et al., 2003). In turn, the photonic LDOS is a key physical factor defining a set of well-known quantum electrodynamic effects: the Purcell effect and the electromagnetic friction (Novotny and Hecht, 2006), the Casimir–Lifshitz forces (Lifshitz and Pitaevskii, 1980), etc.

Thermal radiation in systems with surface plasmons is known to be considerably different from blackbody radiation (Carminati and Greffet, 1999; Henkel et al., 2000; Schegrov et al., 2000). Earlier theoretical studies of SWNTs showed the existence of low-frequency plasmon branches (Lin and Shung, 1993) and the formation of strongly slowed-down electromagnetic surface waves in SWNTs (Slepyan et al., 1999). Such waves define a pronounced Purcell effect in SWNTs (Bondarev et al., 2002) and the potentiality of SWNTs in the development of Cherenkov-type nano-emitters (Batrakov et al., 2006). Geometrical resonances—standing surface waves excited due to the strong reflection from the SWNT tips—qualitatively distinguish SWNTs from the planar structures investigated in Carminati and Greffet (1999), Henkel et al. (2000), and Schegrov et al. (2000). One can expect an essential role of these resonances in the formation of SWNTs' thermal radiation.

5.3.1 Fluctuation-Dissipative Theorem

The fluctuation-dissipative theorem relates the fluctuations of physical quantities to the dissipative properties of the system when it is subjected to an external action. We are interested in the space–time correlation function of the electromagnetic field fluctuations $\langle A_n(\mathbf{r},t)A_m(\mathbf{r}',t')\rangle$, where $\mathbf{A}(\mathbf{r},t)$ is the vector potential of the electromagnetic field. We use the Hamiltonian

gauge, which implies the scalar potential to be equal to zero for the electromagnetic field. For a stationary field, the correlation function depends on the time difference, $t - t'$, only. The Fourier transform of the correlation function is called the cross-spectral density (Joulain et al., 2005):

$$\left\langle A_n(\mathbf{r})A_m^*(\mathbf{r}')\right\rangle_\omega = \int\limits_{-\infty}^{\infty}\left\langle A_n(\mathbf{r},t)A_m(\mathbf{r}',t')\right\rangle e^{i\omega(t-t')}d(t-t'). \quad (5.11)$$

Then the fluctuation-dissipative theorem for the electromagnetic field vector potential is formulated as follows (Lifshitz and Pitaevskii, 1980):

$$\left\langle A_n(\mathbf{r}_1)A_m^*(\mathbf{r}_2)\right\rangle_\omega = \left[\hbar + \frac{2\Theta(\omega,T)}{\omega}\right]\mathrm{Im}\left[G_{nm}(\mathbf{r}_1,\mathbf{r}_2,\omega)\right], \quad (5.12)$$

where
  $\underline{\mathbf{G}}(\mathbf{r}_1,\mathbf{r}_2,\omega)$ is the retarded Green tensor
  $n, m = x, y, z$ designates the Cartesian coordinate system axis
  $\Theta(\omega,T) = \hbar\omega/[\exp(\hbar\omega/k_B T)-1]$, $\hbar$ and k_B are the Planck and Boltzmann constants, respectively

The first term in square brackets is due to the zero vacuum fluctuations, and will be omitted further. Thus, to calculate the intensity of thermal radiation emitted by an SWNT, we elaborate the method of calculation of the electromagnetic field Green tensor in the vicinity of a CNT.

5.3.2 Free-Space Green Tensor

The electromagnetic field Green tensor is defined by the equation

$$(\nabla_{\mathbf{r}_1}\times\nabla_{\mathbf{r}_1}\times-k^2)\underline{\mathbf{G}}(\mathbf{r}_1,\mathbf{r}_2,\omega) = 4\pi\underline{\mathbf{I}}\delta(\mathbf{r}_1-\mathbf{r}_2), \quad (5.13)$$

where
  $\nabla_{\mathbf{r}_1}$ indicates that operator ∇ acts only on the variable r_1 of the Green tensor
  $\underline{\mathbf{I}}$ is the unit tensor
  $k = \omega/c$, ω is the electromagnetic field frequency
  c is the speed of light in vacuum

In general, this equation should be supplemented by boundary conditions.

In the Cartesian coordinate system, Equation 5.13 takes the following index form:

$$\left(\varepsilon_{iln}\varepsilon_{nkj}\frac{\partial^2}{\partial x_{1l}\partial x_{1k}} - k^2\delta_{ij}\right)G_{jm}(\mathbf{r}_1,\mathbf{r}_2,\omega) = 4\pi\delta_{im}\delta(\mathbf{r}_1-\mathbf{r}_2), \quad (5.14)$$

where $x_{1l,k} = x_1, y_1, z_1$ and summation over the repeated indices is assumed. For each index m, Equation 5.14 gives us an independent equation that describes the evolution of the mth column of the Green tensor. Thus, for a given m, the column $G_{nm}(\mathbf{r}_1,\mathbf{r}_2,\omega)$ can formally be considered as a field vector, $\mathbf{G}^{(m)}(\mathbf{r}_1;\mathbf{r}_2)$, induced

at point $\mathbf{r}_1$ by a delta source located at point $\mathbf{r}_2$; here m and $\mathbf{r}_2$ are parameters. Let us introduce the Hertz vector, $\mathbf{\Pi}^{(m)}(\mathbf{r}_1;\mathbf{r}_2)$:

$$\mathbf{G}^{(m)}(\mathbf{r}_1;\mathbf{r}_2) = (k^2 + \nabla\nabla\cdot)\mathbf{\Pi}^{(m)}(\mathbf{r}_1;\mathbf{r}_2) \qquad (5.15)$$

Then we obtain three independent equations instead of Equation 5.14:

$$(\Delta + k^2)\Pi^{(m)}(r_1;r_2) = -\frac{4\pi}{k^2}e_m\delta(r_1 - r_2), \qquad (5.16)$$

where $\mathbf{e}_m = (\delta_{xm},\delta_{ym},\delta_{zm})$ is the basis vector of the Cartesian coordinate system. In the free-space case, the solution of Equation 5.16 is straightforward, (Jackson, 1999) and the free-space Hertz vector has the following form:

$$\mathbf{D}^{(0m)}(\mathbf{r}_1;\mathbf{r}_2) = \frac{1}{k^2}G^{(0)}(\mathbf{r}_1,\mathbf{r}_2,\omega) = \frac{1}{k^2}\frac{e^{ik|\mathbf{r}_1-\mathbf{r}_2|}}{|\mathbf{r}_1-\mathbf{r}_2|}. \qquad (5.17)$$

where

$$G^{(0)}(\mathbf{r}_1,\mathbf{r}_2,\omega) = \frac{e^{ik|\mathbf{r}_1-\mathbf{r}_2|}}{|\mathbf{r}_1-\mathbf{r}_2|} \qquad (5.18)$$

is the free-space Green function. Thus, we obtain the standard expression for the free-space Green tensor (Lifshitz and Pitaevskii, 1980):

$$\mathbf{G}^{(0)}(\mathbf{r}_1,\mathbf{r}_2,\omega) = (\mathbf{I} + k^{-2}\nabla_{\mathbf{r}_1} \otimes \nabla_{\mathbf{r}_1})G^{(0)}(\mathbf{r}_1,\mathbf{r}_2,\omega) \qquad (5.19)$$

with $\nabla_{\mathbf{r}_1} \otimes \nabla_{\mathbf{r}_1}$ as the operator dyadic acting on variables $\mathbf{r}_1$.

5.3.3 Green Tensor in the Vicinity of SWNT

Consider an isolated single-walled CNT of cross-sectional radius R_{cn} and length L, aligned along the z axis of the Cartesian coordinate basis (x, y, z) with the origin in the geometrical center of the CNT (see Figure 5.3). We restrict our consideration to the case $R_{cn} \ll 2\pi/k$, which implies that the incident field should be slowly varied within the CNT cross section.

To calculate the electromagnetic field Green tensor, we should solve Equation 5.13 with the effective boundary conditions (Slepyan et al., 1999) imposed on the SWNT surface. The general solution of the problem can be presented as follows:
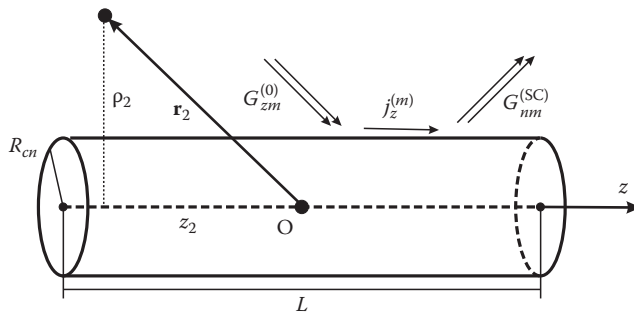

FIGURE 5.3 Free-space Green tensor scattering by an SWNT.

$$\mathbf{G}(\mathbf{r}_1,\mathbf{r}_2,\omega) = \mathbf{G}^{(0)}(\mathbf{r}_1,\mathbf{r}_2,\omega) + \mathbf{G}^{(SC)}(\mathbf{r}_1,\mathbf{r}_2,\omega), \qquad (5.20)$$

where $\mathbf{G}^{(0)}(\mathbf{r}_1,\mathbf{r}_2,\omega)$ is the solution of the inhomogeneous Equation 5.13, for the free-space case and $\mathbf{G}^{(SC)}$ satisfies the equation

$$(\nabla_{\mathbf{r}_1} \times \nabla_{\mathbf{r}_1} \times -k^2)\mathbf{G}^{(SC)}(\mathbf{r}_1,\mathbf{r}_2,\omega) = 0 \qquad (5.21)$$

and boundary conditions on the SWNT surface. From a formal point of view, $\mathbf{G}^{(SC)}$ can be considered as the free-space Green tensor scattered by the SWNT (see Figure 5.3). To calculate the scattered Green tensor, we use the method developed in Lifshitz and Pitaevskii (1980, see problem 1 after paragraph 77). Each column of the free-space Green tensor induces current density $j_z^{(m)}$ on the SWNT surface, which generates the mth column of the scattered Green tensor, $m = x, y, z$. We take into account only the axial component of the induced current due to the fact that the SWNT length is much greater than the SWNT radius. By analogy with the previous section, we introduce three independent scattered Hertz vectors, $\mathbf{\Pi}^{SC(m)}(\mathbf{r}_1;\mathbf{r}_2) = \mathbf{e}_z\Pi^{SC(m)}(\mathbf{r}_1;\mathbf{r}_2)$. Each Hertz vector has only z nonzero component. Further, we omit parameter $\mathbf{r}_2$ in the notation of the Hertz vector to simplify the designations. These Hertz vectors satisfy scalar equations,   AQ2

$$(\Delta + k^2)\Pi^{SC(m)}(\mathbf{r}) = 0, \qquad (5.22)$$

and effective boundary conditions on the CNT surface. Thus we have to solve three equations (Equation 5.22) to calculate scalar quantities $\Pi^{SC(m)}$. We could do this in the arbitrary coordinate system. We use the cylindrical coordinate system (ρ,ϕ,z) in which the effective boundary conditions (Slepyan et al., 1999, 2006) have the simplest form:

$$\left.\frac{\partial\Pi^{SC(m)}(\rho,z)}{\partial\rho}\right|_{\rho=R_{cn}+0} - \left.\frac{\partial\Pi^{SC(m)}(\rho,z)}{\partial\rho}\right|_{\rho=R_{cn}-0}$$

$$= \frac{4\pi}{i\omega}j_z^{(m)}(z;\mathbf{r}_2), \quad -L/2 \le z \le L/2 \qquad (5.23)$$

$$\left.\frac{\partial\Pi^{SC(m)}(\rho,z)}{\partial\rho}\right|_{\rho=R_{cn}+0} - \left.\frac{\partial\Pi^{SC(m)}(\rho,z)}{\partial\rho}\right|_{\rho=R_{cn}-0} = 0, \quad |z| > L/2, \quad (5.24)$$

where

$$j_z^{(m)} = \sigma_{zz}\left[\frac{\partial^2\Pi^{SC(m)}(R_{cn},z)}{\partial z^2} + k^2\Pi^{SC(m)}(R_{cn},z) + G_{zm}^{(0)}(\mathbf{R},\mathbf{r}_2,\omega)\right]. \qquad (5.25)$$

Vector $\mathbf{R}$ designates the point on the CNT surface, and in the cylindrical coordinate system, has the following form: $\{R_{cn},\phi,z\}$. Due to the cylindrical symmetry of the system, the scattered Hertz potential does not depend on the azimuthal variable, ϕ. Here,

$$\sigma_{zz}(\omega) = -\frac{2e^2}{\sqrt{3}\pi\hbar mb(\nu - i\omega)}\sum_{s=1}^{m}\int\frac{\partial\varepsilon_c(p_z,s)}{\partial p_z}\frac{\partial f(p_z,s)}{\partial p_z}dp_z \qquad (5.26)$$

is the axial conductivity of the zigzag SWNT (Slepyan et al., 1999), $f(p_z, s)$ is the equilibrium Fermi distribution, and $v = (1/3) \times 10^{12}$ s^{-1} is the relaxation frequency. Applying the Green theorem (Jackson, 1999) to Equations 5.22 through 5.24, we obtain the integral equations for the normalized axial current density, $j_z^{(m)}(z; \mathbf{r}_2)$, induced on the CNT surface by the incident electric field, $G_{zm}^{(0)}(\mathbf{R}, \mathbf{r}_2, \omega)$ (Nemilentsau et al., 2007):

$$\int_{-L/2}^{L/2} j_z^{(m)}(z'; \mathbf{r}_2) K(z - z') dz' + C_1 e^{-ikz} + C_2 e^{ikz}$$

$$= \frac{1}{2\pi} \int_{-L/2}^{L/2} \frac{e^{ik|z-z'|}}{2ik} \int_0^{2\pi} G_{zm}^{(0)}(\mathbf{R}', \mathbf{r}_2, \omega) d\phi' dz', \qquad (5.27)$$

where $C_{1,2}$ are constants determined by the edge conditions, $j_z^{(m)}(\pm L/2; \mathbf{r}_2) = 0$ (Slepyan et al., 2006),

$$K(z) = \frac{\exp(ik|z|)}{2ik\sigma_{zz}(\omega)} - \frac{2iR_{cn}}{\omega} \int_0^\pi \frac{e^{ikr}}{r} d\phi, \qquad (5.28)$$

and $r = \sqrt{z^2 + 4R_{cn}^2 \sin^2(\phi/2)}$. After three independent integral equations have been solved (Equation 5.27) (for three different values of $m = x, y, z$) and three current density values have been calculated, we again return to the Cartesian coordinate system.

Finally, we can present the solution of the scattering problem in the form of the simple layer potential (Colton and Kress, 1983; Nemilentsau et al., 2007):

$$G_{nm}(\mathbf{r}_1, \mathbf{r}_2, \omega) = G_{nm}^{(0)}(\mathbf{r}_1, \mathbf{r}_2, \omega) + \frac{i\omega R_{cn}}{c^2}$$

$$\times \int_{-L/2}^{L/2} j_z^{(m)}(z; \mathbf{r}_2) \int_0^{2\pi} G_{nz}^{(0)}(\mathbf{r}_1, \mathbf{R}, \omega) d\phi dz. \qquad (5.29)$$

While deriving Equation 5.29, we assumed the incident field source distance from the CNT farther than its radius; therefore, we can neglect the of the current $j_z^{(m)}$ dependence on the azimuthal variable, ϕ.

Equation 5.29 with an arbitrary $j_z^{(m)}$ satisfies the aforementioned equation for the retarded Green tensor and the radiation condition at $|\mathbf{r}_1 - \mathbf{r}_2| \to \infty$. Peculiar electronic properties of CNTs (Dresselhaus et al., 2000) influence the Green tensor through the axial conductivity $\sigma_{zz}(\omega)$ (for details, see Slepyan et al. (1999)). The index m and the variable $\mathbf{r}_2$ appear in Equations 5.29 and 5.27 only as parameters. Note that these equations, as they couple the Green tensor of the system considered and the free-space Green tensor, play the role of the Dyson equation for CNTs.

It is important that the role of scattering by CNTs *is not reduced* to a small correction to the free-space Green tensor. This means that the Born approximation conventionally used for solving the Dyson equation (Lifshitz and Pitaevskii, 1980) becomes inapplicable to our case. Because of this, the direct

numerical integration of Equation 5.27 has been performed with integral operators approximated by a quadrature formula and subsequent transition to a matrix equation.

5.3.4 Thermal Radiation Calculation

Let us calculate the thermal radiation of a hot SWNT placed into an optically transparent cold environment. As the fluctuation-dissipative theorem (Equation 5.12) is applicable only at thermal equilibrium, we cannot directly apply it in this case.

To solve the problem, let us consider in more detail the case when the SWNT is in thermal equilibrium with the environment. At thermal equilibrium, the thermal fluctuation field in the system is the superposition of three different fields: thermal electromagnetic field radiated by the SWNT itself; blackbody radiation of the surrounding medium in the absence of the CNT, $\mathbf{A}^{(0)}$; and the field $\mathbf{A}^{(s)}$ resulting from the scattering of radiation of the medium by the SWNT. In the case of the cold medium, the only electromagnetic field radiated by the SWNT remains. Thus, to calculate the thermal radiation of the hot SWNT placed in the cold medium, we should calculate the total thermal electromagnetic field radiated in the equilibrium and separate the blackbody contribution.

The thermal radiation intensity in equilibrium is easily calculated by substituting Equation 5.29 for the electromagnetic field Green tensor to Equation 5.12 for the fluctuation-dissipative theorem. To separate the blackbody radiation contribution, we use the method developed in Lifshitz and Pitaevskii (1980, see problems after Sect. 77). We introduce the blackbody radiation vector potential,

$$\mathbf{A}^{(B)}(\mathbf{r}) = \mathbf{A}^{(0)}(\mathbf{r}) + \mathbf{A}^{(s)}(\mathbf{r}), \qquad (5.30)$$

and calculate the correlator:

$$\left\langle A_n^{(B)}(\mathbf{r}_1) A_m^{(B)*}(\mathbf{r}_2) \right\rangle_\omega \equiv D_{nm}^{(B)}(\mathbf{r}_1, \mathbf{r}_2, \omega). \qquad (5.31)$$

Then, the electric field intensity of the SWNT thermal radiation in the case when the SWNT temperature is much higher that the temperature of the surrounding medium, $I_\omega(\mathbf{r}_0) = |\mathbf{E}(\mathbf{r}_0)|^2$ is given, in view of the relation $E_n = -ikA_n$, by

$$I_\omega(\mathbf{r}_0) = k^2 \sum_{n=1}^3 \left[\left\langle |A_n(\mathbf{r}_0)|^2 \right\rangle_\omega - D_{nn}^{(B)}(\mathbf{r}_0, \mathbf{r}_0, \omega) \right]. \qquad (5.32)$$

To calculate the blackbody radiation correlator, we should calculate the scattered vector potential, $A^{(s)}$. To do this, we should solve Equations 5.22 through 5.25 with $A^{(0)}$ instead of the free-space Green tensor, $G_{zm}^{(0)}$, in Equation 5.25. By analogy with Equation 5.29, the vector $A_n^{(B)}(\mathbf{r}_1)$, potential, is written as

$$A_n^{(B)}(\mathbf{r}_1) = A_n^{(0)}(\mathbf{r}_1) + \frac{R_{cn}}{c} \int_{-L/2}^{L/2} j(z) \int_0^{2\pi} G_{nz}^{(0)}(\mathbf{r}_1, \mathbf{R}, \omega) d\phi dz, \qquad (5.33)$$

where the current density, $j(z)$, induced on the SWNT surface by the free-space fluctuation electromagnetic field, $A^{(0)}$, is the solution of the integral equation

AQ3

$$\int_{-L/2}^{L/2} K(z-z')j(z')dz' + C_1 e^{-ikz} + C_2 e^{ikz} = \frac{1}{2}\int_{-L/2}^{L/2} A_z^{(0)}(\mathbf{R}')e^{ik|z-z'|}dz'.$$

(5.34)

The second term in Equation 5.33 describes scattering of the free-space blackbody radiation by the SWNT. To calculate $D_{nm}^{(B)}$, we utilize Equation 5.33 and take into account that the correlator, $\left\langle A_n^{(0)}(\mathbf{r}_1)A_m^{(0)\star}(\mathbf{r}_2)\right\rangle_\omega$ is defined by Equation 5.12 with the free-space Green tensor, $\mathbf{G}_{nm}^{(0)}(\mathbf{r}_1,\mathbf{r}_2,\omega)$, on the right-hand side.

5.3.5 Numerical Results

In this section, we present the results of the numerical calculations of the thermal radiation emitted by metallic (15,0) (see Figure 5.4) and semiconducting (23,0) SWNTs (see Figure 5.5). The following parametrization of the radius vector is used throughout this section:

$$\mathbf{r} = \{\rho,\phi,z\} = \mathbf{e}_x\rho\cos\phi + \mathbf{e}_y\rho\sin\phi + \mathbf{e}_z z.$$

(5.35)

The spectra of the thermal radiation from the SWNT (15,0) at different distances from the SWNT axis are presented in Figure 5.4a and b presents one of the spectra in the logarithmic scale. The spectrum depicted in Figure 5.4a demonstrates a number of equidistant discrete spectral lines with decreasing intensities superimposed by the continuous background. Such a structure
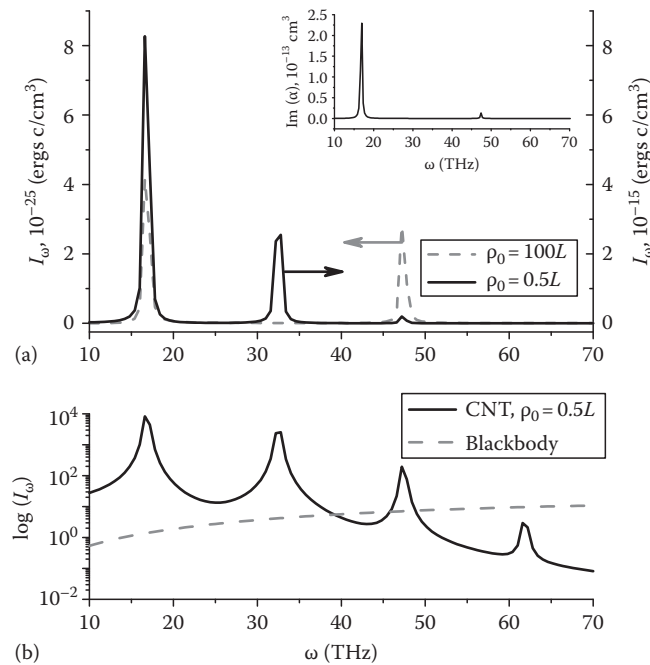

FIGURE 5.4 (a) Thermal radiation spectra of a metallic (15,0) SWNT. $\mathbf{r}_0 = \{100\,L,\phi_0,0\}$ (dashed line, left ordinate axis) and $\mathbf{r}_0 = \{0.5\,L,\phi_0,0\}$ (solid line, right ordinate axis); ϕ_0 is arbitrary; $T = 300\,$K; and $L = 1\,\mu$m. The inset presents the CNT's polarizability. (b) Thermal radiation from CNT in the near-field zone (solid line) compared to blackbody radiation, $I_\omega^{(B)}(\mathbf{r}_0) = 4\omega^2\Theta(\omega,T)/c^3$ (dashed line). (From Nemilentsau, A.M. et al., *Phys. Rev. Lett.*, 99, 147403, 2007.)
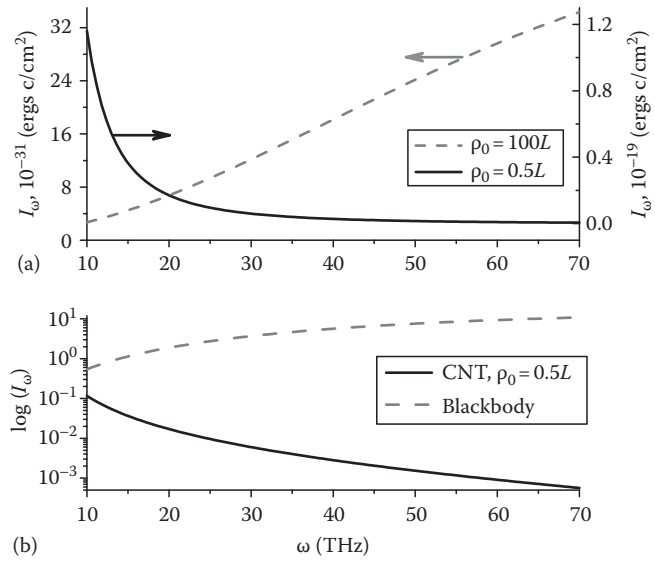

FIGURE 5.5 Same as Figure 5.4, but for the (23,0) semiconducting SWNT. (From Nemilentsau, A.M. et al., *Phys. Rev. Lett.*, 99, 147403, 2007.)

is inherent to spectra both in the far-field (dashed line) and near-field (solid line) zones. The peculiarity of the near-field zone is the presence of additional spectral lines absent in the far-field zone. Thus, the thermal radiation spectra presented in the figure qualitatively differ from both blackbody radiation (Lifshitz and Pitaevskii, 1980) and radiation of semi-infinite SiC samples (Schegrov et al., 2000). In the latter case, the discrete spectrum is observed only in the near-field zone (Schegrov et al., 2000).

The comparison of the thermal radiation and the SWNT's polarizability spectra (Slepyan et al., 2006) depicted in Figure 5.4a reveals the coincidence in the far-field zone of the thermal radiation resonances and the polarizability resonances. The latest are the *dipole* geometrical resonances of surface plasmons (Slepyan et al., 2006) defined by the condition $\mathrm{Re}[\kappa(\omega)]L \cong \pi(2s-1)$, with $\kappa(\omega)$ as the plasmon wavenumber; s is a positive integer. It should be noted that the polarizability (and the thermal radiation) resonances are found to be significantly shifted to the red as compared to the perfectly conducting wire of the same length, because of the strong slowing-down of surface plasmons in SWNTs: $\mathrm{Re}[\kappa(\omega)]/k \approx 100$ (Slepyan et al., 1999). In particular, for $L = 1\,\mu$m, the geometrical resonances fall into the THz frequency range. The attenuation is small in a wide frequency range below the interband transitions. Additional spectral lines in the near-field zone are described by the condition $\mathrm{Re}[\kappa(\omega)]L \cong 2\pi s$. We refer to these resonances as *quadrupole* geometric resonances because the current density distribution for these modes is antisymmetrical with respect to $z = 0$ and, consequently, the dipole component of their field is identically zero. Thus, the resonant structure of the thermal radiation spectra is determined by the finite-length effects and also depends on the peculiar conductivity of SWNTs. Note that a similar structure of the thermal radiation spectra is predicted for the two-dimensional electron gas (Richter et al., 2007).

Resonances in the article by Richter et al. (2007) are due to the excitations of other physical nature—optical phonon modes of the barrier material.

The presence of singled out resonances illustrated in Figure 5.4a allows us to propose metallic SWNTs as far-field and near-field *thermal antennas* for the THz range (optical thermal antennas based on photonic crystals have recently been considered in the article by Laroche et al. (2006) and Florescu et al. (2007). Taking into account the high temperature stability of SWNTs, the SWNT thermal antennas can be excited by Joule heating from the direct electric current. Low-frequency alteration of the current allows the amplitude modulation of thermal emission and, consequently, allows the use of the thermal emission for information transmission (similar to modulated RF fields in present-day radioengineering). The scattering pattern of the thermal antenna can be calculated using the approaches developed in Hanson (2005) and Slepyan et al. (2006) and is found to be partially polarized and directional. A polarization of the thermal radiation from bundles of multi-walled SWNTs has been observed experimentally in Li et al. (2003). The blackbody spectrum reported in Li et al. (2003) is due to the inhomogeneous broadening originated from the SWNT length and radius dispersion and multi-walled effects. Moreover, the observation was made above the frequency range of surface plasmons.

According to the article by Hanson (2005), Slepyan et al. (2006), and Burke et al. (2006) the maximal efficiency of vibrator SWNT antennas is reached at frequencies of the surface-plasmon dipole resonances. Figure 5.4a shows that the intensities of spectral lines of the thermal radiation go down with the resonance number much slowly than the polarizability peaks. This means that the signal–noise ratio for the SWNT-based antennas is maximal for the first resonance and decreases fast with the resonance number.

As different from metallic SWNTs, semiconducting ones do not reveal isolated resonances in both far-field and near-field zones (see Figure 5.5 as an illustration). Such a peculiarity can easily be understood by accounting for the strong attenuation of surface plasmons in semiconducting SWNTs, whereas the slowing down remains of the same order. That is why in this case the Q factor of geometrical resonances turns out to be substantially smaller and the resonances do not manifest themselves as separated spectral lines. In the same way, the thermal radiation intensity of semiconducting SWNTs is substantially smaller than that of metallic ones and displays qualitatively different spectral properties in the near-field zone: monotonous growth of the intensity with frequency inherent to the far-field zone changes into monotonous declining (see Figure 5.5a). As the thermal spectra are strongly dependent on the SWNT conductivity type and length, the near-field thermal radiation spectroscopy proposed in Schegrov et al. (2000) for testing the surface-plasmon structures can be expanded to SWNTs.

Figure 5.5b demonstrates that in the frequency range considered, the black-body radiation intensity considerably exceeds the thermal radiation of semiconducting SWNTs: $I_\omega \ll I_\omega^{(B)}$. In the regions between geometrical resonances the same property is

inherent to metallic SWNTs (see Figure 5.4b). This means that CNTs as building blocks for nanoelectronics and nanosensorics possess uniquely low thermal noise and, thus, provide *high electromagnetic compatibility on the nanoscale*: Their contribution to the electromagnetic fluctuations in nanocircuits is negligibly small as compared to the contribution of dielectric substrate. More generally, the latter example illustrates the peculiarity of the electromagnetic compatibility problem on the nanoscale, motivating future research investments into the problem.

Next, we have studied the spatial structure of the electromagnetic fluctuations near SWNTs, characterized by the normalized first-order correlation tensor:

$$g_{nm}^{(1)}(\mathbf{r}_1,\mathbf{r}_2,\omega) = \frac{\left\langle A_n(\mathbf{r}_1) A_m^*(\mathbf{r}_2) \right\rangle_\omega}{\sqrt{\left\langle |A_n(\mathbf{r}_1)|^2 \right\rangle_\omega \left\langle |A_m(\mathbf{r}_2)|^2 \right\rangle_\omega}}. \qquad (5.36)$$

The axial–axial component of this tensor is depicted in Figure 5.6. The figure clearly displays the distinctive behavior of the correlation in the far- and near-field zones. In the vicinity of geometrical resonances, where $\text{Re}(\kappa)L \sim 1$, the near-field zone is defined by the condition $\rho \lesssim L$. Because of strong slowing down of surface plasmons in SWNTs (Slepyan et al., 1999), the latter condition corresponds to $k\rho \ll 1$; for the first geometrical resonance in the 1 pm length SWNT, depicted in Figure 5.6, $k\rho \lesssim 0.06$. Thus, the figure demonstrates a strong correlation between points inside the near-field zone (curves 1–3) and its fast falling down as ρ increases, indicating a weak correlation between near- and far-field zones. Physically, this is related to the fact that the dominant field component in the near-field zone is a nonradiative surface plasmon while radiative modes dominate in the far-field zone. The latter condition also explains that in the far-field zone, the correlation function is well approximated by the blackbody radiation law, $\sin(k\rho)/k\rho$, with the radial correlation length $\sim 1/k$. Note,
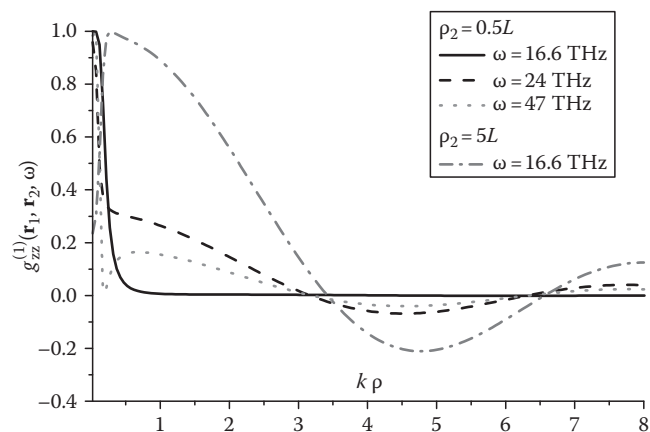
FIGURE 5.6 First-order correlation function, $g_{zz}^{(1)}(\mathbf{r}_0,\mathbf{r}_2,\omega)$, for a metallic (15,0) SWNT in radial direction. $\mathbf{r}_1 = \{\rho,\phi,0\}$ with an arbitrary ϕ. Curves 1–3 depict correlation for $\mathbf{r}_2 = \{0.5 L,\phi,0\}$, while curve 4 presents the case $\mathbf{r}_2 = \{5 L,\phi,0\}$. (Nemilentsau, A.M. et al., *Phys. Rev. Lett.*, 99, 147403, 2007.)

AQ4

AQ5

that the long-range spatial correlation characteristics for surface-plasmon planar structures (Carminati and Greffet, 1999; Henkel et al., 2000) are found to be absent in SWNTs. The reason is that SWNTs in the vicinity of geometrical resonances are electrically small oscillators ($kL \ll 1$) with wide scattering patterns (Slepyan et al., 2006).

5.4 Quasi-Metallic Carbon Nanotubes as Terahertz Emitters

The next scheme of the THz generation (Kibis and Portnoi, 2005; Kibis et al., 2007) is based on the electric-field an induced heating of electron gas in an SWNT, resulting in the inversion of population of optically active states with the energy difference within the THz spectrum range. It is well known that the elastic backscattering processes in metallic SWNTs are strongly suppressed (Ando et al., 1997), and in a high-enough electric field charge carriers can be accelerated up to the energy allowing emission of optical/zone-boundary phonons. At this energy, corresponding to the frequency of about 40 THz, the major scattering mechanism switches on abruptly, resulting in current saturation(Yao et al., 2000; Freitag et al., 2004; Javey et al., 2004; Park et al., 2004; Perebeinos et al., 2005). As will be shown hereafter, for certain types of carbon nanotubes, the heating of electrons to the energies below the phonon-emission threshold results in a spontaneous THz emission with the peak frequency controlled by an applied voltage.

The electron energy spectrum, $\varepsilon(k)$ (Equation 5.8), of a metallic SWNT in the vicinity of the Fermi energy linearly depends on the electron wave vector, k, and has the form $\varepsilon(k) = \pm \hbar v_F |k - k_0|$, where $v_F \approx 9.8 \times 10^5$ m/s is the Fermi velocity of graphene, which corresponds to the commonly used tight-binding matrix element, $\gamma_0 = 3.033$ eV (Saito et al., 1998; Reich et al., 2004). Here and in what follows, the zero of energy is defined as the Fermi

energy position in the absence of an external field. When the voltage, V, is applied between the SWNT ends, the electron distribution is shifted in the way shown by the thick lines in Figure 5.7a, corresponding to the filled electron states.

This shift results in inversion of population and, correspondingly, in optical transitions between filled states in the conduction band and empty states in the valence band. The spectrum of optical transitions is determined by the distribution function for hot carriers that, in turn, depends on the applied voltage and scattering processes in the SWNT. It is well known that the major scattering mechanism in SWNTs is due to the electron–phonon interaction (Yao et al., 2000; Javey et al., 2004; Park et al., 2004; Perebeinos et al., 2005). Since the scattering processes erode the inversion of electron population, an optimal condition for observing the discussed optical transitions takes place when the length of the SWNT $L < l_{ac}$, where the electron mean-free path for acoustic phonon scattering is $l_{ac} \approx 2\,\mu$m (Park et al., 2004). Further, only such short SWNTs with ideal Ohmic contacts (Javey et al., 2004) are considered in the ballistic transport regime, when the energy acquired by the electron on the whole length of the tube, $\Delta\varepsilon = eV$, does not exceed the value of $\hbar\Omega = 0.16$ eV at which a fast emission of high-energy phonons begins (Park et al., 2004). In this so-called low-bias regime (Yao et al., 2000; Javey et al., 2004; Park et al., 2004), in which the current in the nanotube is given by the Büttiker–Landauer-type formula, $I \approx (4e^2/h)V$, the distribution function of hot electrons is

$$f_e(k) = \begin{cases} 1, & 0 < k - k_0 < \Delta\varepsilon / 2\hbar v_F \\ 0, & k - k_0 > \Delta\varepsilon / 2\hbar v_F \end{cases}. \qquad (5.37)$$

The distribution function for hot holes, $f_h(k)$, has the same form as $f_e(k)$.

Let us select an SWNT with crystal structure most suitable for the observation of the discussed effect. First, the required nanotube should have metallic conductivity, and, second, the optical
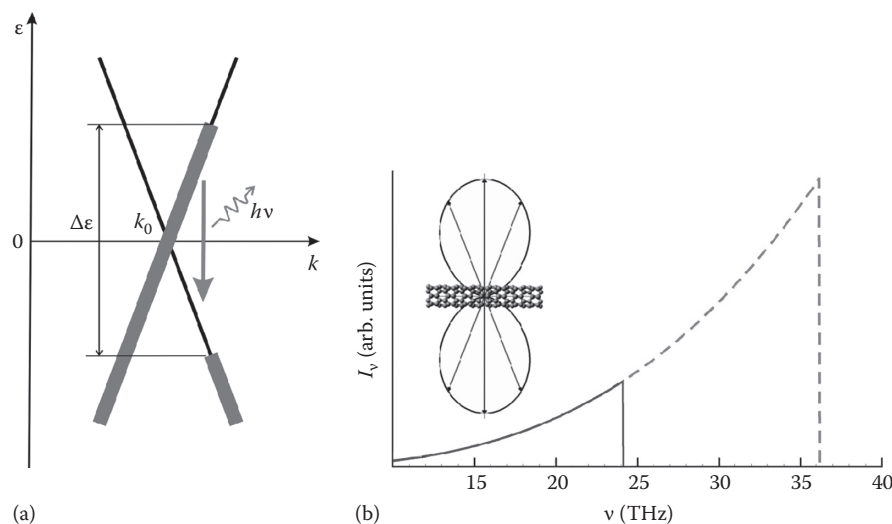

FIGURE 5.7 (a) The scheme of THz photon generation by hot carriers in quasi-metallic SWNTs. (b) The spectral density of spontaneous emission as a function of frequency for two values of applied voltage: solid line for $V = 0.1$ V and dashed line for $V = 0.15$ V. The inset shows the directional radiation pattern of the THz emission with respect to the nanotube axis. (From Portnoi, M.E. et al., *Superlattices Microstruct.*, 43, 399, 2008.)

transitions between the lowest conduction subband and the top valence subband should be allowed. SWNTs having a true metallic energy band structure, for which the energy gap is absent for any SWNT radius, are armchair (*n*,*n*) SWNTs only (Kane and Mele, 1997; Ouyang et al., 2001; Reich et al., 2004; Gunlycke et al., 2006; Li et al., 2006). However, for armchair SWNTs, the optical transitions between the first conduction and valence subbands are forbidden (Milošević et al., 2003; Jiang et al., 2004). So, for the observation of THz generation, it is suitable to use the so-called quasi-metallic (*n*, *m*) SWNTs with *n* − *m* = 3*p*, where *p* is a nonzero integer. These nanotubes, which are gapless within the frame of a simple zone-folding model of the π-electron graphene spectrum (Saito et al., 1998), are in fact narrow-gap semiconductors due to curvature effects. Their bandgap is given by $\varepsilon_g = \hbar v_F b \cos 3\theta / (8 R_{cn}^2)$ (Kane and Mele, 1997; Gunlycke et al., 2006). It can be seen from the expression for ε_g that the gap is decreasing rapidly with the increasing nanotube radius. For large values of R_{cn}, this gap can be neglected even in the case of moderate applied voltages due to Zener tunneling of electrons across the gap. It is easy to show in a fashion similar to the original Zener's work (Zener, 1934) that the tunneling probability in quasi-metallic SWNTs is given by $\exp(-\alpha\varepsilon_g^2/eE\hbar v_F)$, where α is a numerical factor close to unity.* For example, for a zigzag (30,0) SWNT the gap is $\varepsilon_g \approx 6$ meV, and the Zener breakdown takes place for the electric field $E \sim 10^{-1}$ V/μm. Since almost the whole voltage drop in the ballistic regime occurs within the few-nanometer regions near the contacts (Svizhenko and Anantram, 2005), a typical bias voltage of 0.1 V corresponds to an electric field, which is more than sufficient to achieve a complete breakdown. In what follows, all calculations are performed for a zigzag (3*p*, 0) SWNT of large enough radius, R_{cn}, and for applied voltages exceeding the Zener breakdown, so that the finite-gap effects can be neglected. The obtained results can be easily generalized for any quasi-metallic large-radius SWNT.

Optical transitions in SWNTs have been a subject of extensive research (see, e.g., Grüneis et al., 2003; Milošević et al., 2003; Jiang et al., 2004; Popov and Henrard, 2004; Saito et al., 2004; Goupalov, 2005; Oyama et al., 2006). Let us treat these transitions using the results of the nearest-neighbor orthogonal 7r-electron tight-binding model (Saito et al., 1998). Despite its apparent simplicity and well-known limitations, this model has been extremely successful in describing low-energy optical spectra and electronic properties of SWNTs (see, e.g., Sfeir et al. (2006) for one of the most recent manifestations of this model's success). The main goal is to calculate the spectral density of spontaneous emission, I_v, which is the probability of optical transitions per unit time for the photon frequencies in the interval (ν, ν + *d*ν) divided by *d*ν. In the dipole approximation (Berestetskii et al., 1997), this spectral density is given by

---

* For the energy spectrum near the band edge given by $\varepsilon = \pm\left[\varepsilon_g^2/4 + \hbar^2 v_F^2(k-k_0)^2\right]^{1/2}$, it can be shown that α = π/4.

$$I_v = \frac{8\pi e^2 v}{3c^3}\sum_{i,f} f_e(k_i)f_h(k_f)\left|\left\langle\Psi_f\,|\,\hat{v}_z\,|\,\Psi_i\right\rangle\right|^2\delta(\varepsilon_i - \varepsilon_f - h v). \quad (5.38)$$

Equation 5.38 contains the matrix element of the electron velocity operator. In the frame of the tight-binding model, this matrix element for optical transitions between the lowest conduction and the highest valence subbands of the (3*p*, 0) zigzag SWNT can be written as (Jiang et al., 2004; Grüneis et al., 2003)

$$\left\langle\Psi_f\,|\,\hat{v}_z\,|\,\Psi_i\right\rangle = \frac{\hbar\omega_{if}}{8}\delta_{k_f,k_i}, \quad (5.39)$$

where $\hbar\omega_{if} = \varepsilon_i - \varepsilon_f$ is the energy difference between the initial (*i*) and the final (*f*) state. These transitions are associated with the light polarized along the nanotube axis *z*, in agreement with the general selection rules for SWNTs (Milošević et al., 2003). Substituting Equation 5.39 in Equation 5.38 and performing necessary summation, we get AQ6

$$I_v = Lf_e(\pi v/v_F)f_h(\pi v/v_F)\frac{\pi^2 e^2 b^2 v^3}{6c^3\hbar v_F}. \quad (5.40)$$

Equation 5.40 has broader applicability limits than the considered case of $L < l_{ac}$ and $eV < \hbar\Omega$, in which the distribution functions for electrons and holes are given by Equation 5.37. In the general case, there is a strong dependence of I_v on the distribution functions, which have to be calculated taking into account all the relevant scattering mechanisms (Yao et al., 2000; Javey et al., 2004; Park et al., 2004; Perebeinos et al., 2005). In the discussed ballistic regime, the spectral density has a universal dependence on the applied voltage and photon frequency for all quasi-metallic SWNTs. In Figure 5.7b, the spectral density is shown for two values of the voltage. It is clearly seen that the maximum of the spectral densities of emission has a strong voltage dependence and lies in the THz frequency range for experimentally attainable voltages. The directional radiation pattern, shown in the inset of Figure 5.7b, reflects the fact that the emission of light polarized normally to the nanotube axis is forbidden by the selection rules for the optical transitions between the lowest conduction subband and the top valence subband.

For some device applications, it might be desirable to emit photons propagating along the nanotube axis, which is possible in optical transitions between the SWNT subbands characterized by angular momenta differing by one (Milošević et al., 2003; Reich et al., 2004). To achieve the emission of these photons by electron heating, it is necessary to have an intersection of such sub-bands within the energy range accessible to electrons accelerated by attainable voltages. From the analysis of different types of SWNTs, it follows that the intersection is possible, for example, for the lowest conduction subbands in several semi-conducting zigzag nanotubes and in all armchair nanotubes. However, for an effective THz emission from these nanotubes, it is necessary to move the Fermi level very close to the subband intersection point (Kibis and Portnoi, 2005). Therefore, obtaining the THz

emission propagating along the nanotube axis is a more difficult technological problem than generating the emission shown in Figure 5.7b.

5.5 Chiral Carbon Nanotubes as Frequency Multipliers

Another proposal for using SWNTs for THz applications (Kibis et al., 2008; Portnoi et al., 2008) is based on chiral nanotubes, which represent natural super-lattices. For example, a (10, 9) SWNT has a radius that differs from the radius of the most commonly studied (10,10) nanotube by less than 5%, whereas a translational period, *T*, along the axis of the (10,9) SWNT is almost 30 times larger than the period of the (10, 10) nanotube. Correspondingly, the first Brillouin zone of the (10, 9) nanotube is 30 times smaller than the first zone for the (10,10) tube. However, such a Brillouin zone reduction cannot influence electronic transport unless there is a gap opening between the energy subbands resulting from the folding of the graphene spectrum. It can be shown that an electric field normal to the nanotube axis opens noticeable gaps at the edge of the reduced Brillouin zone, thus turning a long-period nanotube of certain chirality into a "real" superlattice. This gap opening is a general property of chiral nanostructures exposed to a transverse electric field (Kibis et al., 2005a,b; Kibis and Portnoi, 2007, 2008). The field-induced gaps are most pronounced in (*n*, 1) SWNTs (Kibis et al., 2005a,b; Portnoi et al., 2006, 2008).

Figure 5.8a shows the opening of an electric-field induced gap near the edge of the Brillouin zone of a (6,1) SWNT. This gap opening results in the appearance of a negative effective-mass region in the nanotube energy spectrum. The typical electron energy in this part of the spectrum of 15 meV is well below the optical phonon energy $\hbar\Omega \approx 160$ meV, so that it can easily be accessed in moderate heating electric fields. The negative effective mass results in NDC, as can be seen from Figure 5.8b. The NDC characteristic presented in Figure 5.8b is calculated assuming the energy-independent scattering time $\tau = 1$ ps. However, when the carrier energy reaches the optical or edge-phonon energy, the scattering time, τ, increases abruptly. This results in more pronounced NDC, which can be used for generating electromagnetic radiation in the THz range. In fact, recent Monte Carlo simulations (Akturk et al., 2007a,b) show that the phonon-induced effects alone might result in THz current oscillations in SWNTs.

The effect of the negative effective mass in chiral nanotubes (Portnoi et al., 2008) not only results in NDC but also leads to an efficient frequency multiplication in the THz range. The results of calculations of the electron velocity in the presence of the time-dependent longitudinal electric field are presented in Figure 5.9. One of the advantages of a frequency multiplier based on chiral SWNTs, in comparison with the conventional superlattices (Alekseev et al., 2006), is that the dispersion relation in such a system can be controlled by the transverse electric field, $E_\perp$.

5.6 Armchair Nanotubes in a Magnetic Field as Tunable THz Detectors and Emitters

The problem of detecting THz radiation is known to be at least as challenging as creating reliable THz sources. The proposal of a novel detector (Kibis et al., 2008; Portnoi et al., 2008) is based on several features of truly gapless (armchair) SWNTs. The main property to be utilized is opening of a bandgap in these SWNTs in a magnetic field along the nanotube axis (Saito et al., 1998; Reich et al., 2004). For a (10,10) SWNT, this gap corresponds to approximately 1.6 THz in the field of 10 T. For attainable magnetic fields, the gap grows linearly with increasing both the magnetic field and the nanotube radius. It can be shown (Portnoi et al., 2008) that the same magnetic field also allows dipole optical transitions between the top valence subband and the lowest conduction subband, which are strictly forbidden in armchair SWNTs without the field (Milošević et al., 2003).

In Figure 5.10, it is shown how the energy spectrum and matrix elements of the dipole optical transitions polarized along the nanotube axis are modified in the presence of a longitudinal magnetic field. In the frame of the nearest-neighbor tight-binding model, one can show that for a (*n*,*n*) armchair nanotube the squared matrix element of the velocity operator between the states at the edge of the gap opened by the magnetic field is given by a simple analytic expression:
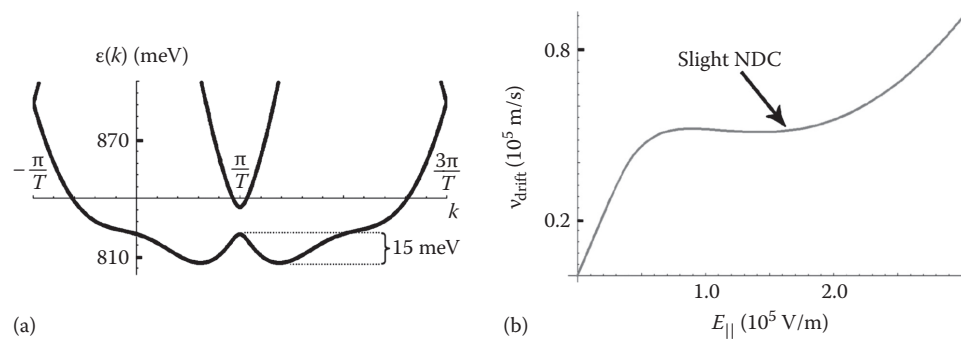

(a)

(b)

FIGURE 5.8 (a) Energy spectrum of the (6,1) SWNT in a transverse electric field, $E_\perp = 4$ V/nm. (b) The electron drift velocity in the lowest conduction subband of a (6, 1) SWNT as a function of the longitudinal electric field, in the presence of acoustic phonon scattering. (From Portnoi, M.E. et al., *Superlattices Microstruct.*, 43, 399, 2008.)
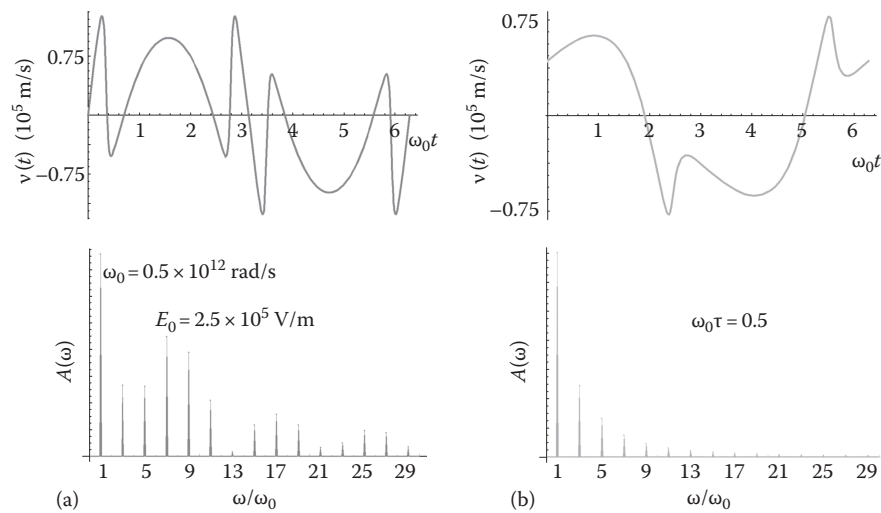
FIGURE 5.9 Time dependence of the electron velocity in the lowest conduction subband of a (6,1) SWNT under the influence of a pump harmonic longitudinal electric field, $E_\parallel(t) = E_0\sin(\omega_0 t)$, and its correspondent spectral distribution, $A(\omega)$: (a) in the ballistic transport regime and (b) in the presence of scattering with the relaxation time $\tau = 10^{-12}$ s. (From Portnoi, M.E. et al., *Superlattices Microstruct.*, 43, 399, 2008.)
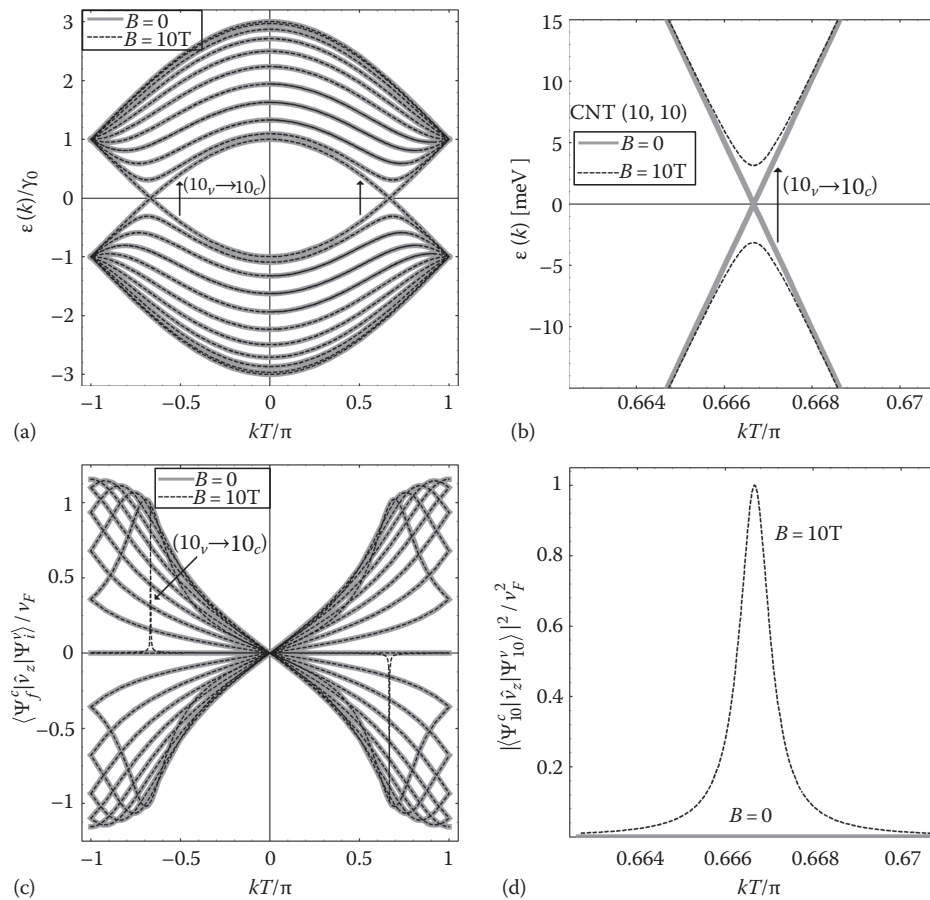

FIGURE 5.10 (a) Band structure of a (10, 10) nanotube, with and without an external magnetic field along the nanotube axis. (b) Detailed view of the gap, which is opened between the top valence subband and the lowest conduction subband in an external field, $B = 10$ T. (c) The change in the matrix elements of the dipole optical transitions, for the light polarized along the SWNT axis, due to the introduction of the external magnetic field. The only appreciable change is in the appearance of a high, narrow peak associated with the transition $(10_v \rightarrow 10_c)$, which is not allowed in the absence of the magnetic field. Here and in what follows, the energy subbands are numbered in the same way as in Saito et al. (1998). (d) Dependence of the squared dipole matrix element for the transition $(10_v \rightarrow 10_c)$ on the 1D wave vector, k, with and without an external magnetic field. (From Portnoi, M.E. et al., *Superlattices Microstruct.*, 43, 399, 2008.)
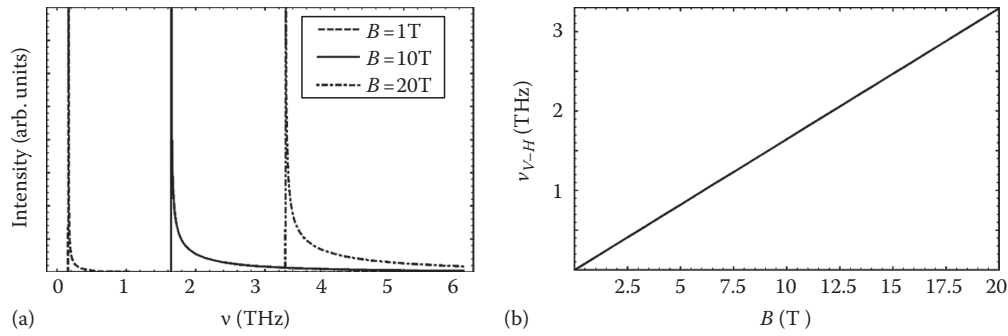
FIGURE 5.11 (a) Calculated photon absorption spectra for a (10,10) SWNT, for three different magnetic field values. The absorption intensity is proportional to the product of $\left|\left\langle \Psi_{10}^{v} | \hat{v}_z | \Psi_{10}^{c} \right\rangle\right|^2$ and the joint DOS. (b) Dependence of the position of the peak in the absorption intensity associated with the Van Hove singularity on the magnetic field. (From Portnoi, M.E. et al., *Superlattices Microstruct.*, 43, 399, 2008.)
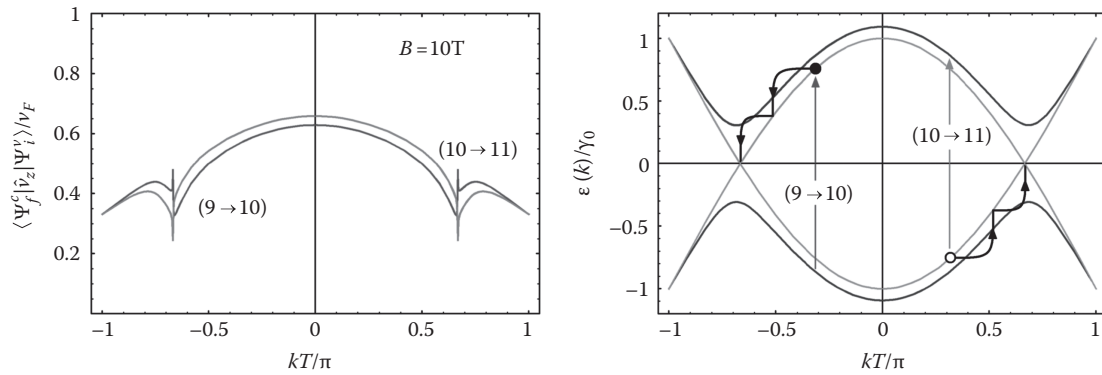

FIGURE 5.12 A scheme for creating a population inversion between the lowest conduction subband and the top valence subband of an armchair SWNT in a magnetic field. The left plot shows the calculated matrix elements of the relevant dipole optical transitions polarized normally to the axis of a (10, 10) SWNT. The right plot shows several energy subbands closest to the Fermi level and illustrates the creation of photoexcited carriers and their nonradiative thermalization. (From Portnoi, M.E. et al., *Superlattices Microstruct.*, 43, 399, 2008.)

$$\left|\left\langle \Psi_n^{\upsilon} | \hat{v}_z | \Psi_i^c \right\rangle\right|^2 = \frac{4}{3}\left[1 - \frac{1}{4}\cos^2\left(\frac{f}{n}\pi\right)\right]v_F^2, \qquad (5.41)$$

where $f = eBR^2/(2\hbar)$. For experimentally attainable magnetic fields, when the magnetic flux through the SWNT is much smaller than the flux quantum, the absolute value of the velocity operator is close to v_F. Equation 5.41 is relevant to the transitions between the highest valence subband and the lowest conduction subband only for $f \leq 1/2$, since for the higher values of/the order of the nanotube subbands is changed. Notably, the same equation allows to obtain the maximum value of the velocity operator in any armchair SWNT for the transitions polarized along its axis: this value cannot exceed $2v_F / \sqrt{3}$ (see Figure 5.10c).

The electron (hole) energy spectrum near the bottom (top) of the bandgap produced by the magnetic field is parabolic as a function of a carrier momentum along the nanotube axis. This dispersion results in a Van Hove singularity in the reduced DOS that, in turn, leads to a very sharp absorption maximum near the band edge and, correspondingly, to a very

high sensitivity of the photocurrent to the photon frequency (see Figure 5.11).

Notably, the same effect can be used for the generation of a very narrow emission line having the peak frequency tunable by the applied magnetic field. A population inversion can be achieved, for example, by optical pumping with the light polarized normally to the nanotube axis, as shown in Figure 5.12.

5.7 Conclusion

In this chapter we have demonstrated several novel schemes for the emission and detection of the THz radiation by the SWNTs.

We have demonstrated that intensity spectra of the thermal electromagnetic field emitted by metallic SWNTs of micron length reveal resonances in the THz range. These resonances are the geometrical resonances of the surface plasmons in SWNTs. It is quite important that we could vary the resonance frequency by changing the SWNT length or conductivity. The predicted effect allows to formulate the conception of, metallic SWNT as a thermal antenna in the THz range and is of importance for the SWNT spectroscopy, the nanoantenna design, the high-resolution

near-field optical microscopy, and the thermal noise control in nanocircuits.

We also have demonstrated that a quasi-metallic carbon nanotube can emit the THz radiation when potential difference is applied to its ends. The typically required voltages and nanotube parameters are similar to those available in the state-of-the-art transport experiments. The maximum of the spectral density of emission is shown to have a strong voltage dependence, which is universal for all quasi-metallic carbon nanotubes in the ballistic regime. Therefore, the discussed effect can be used for creating a THz source with frequency controlled by the applied voltage. Appropriately arranged arrays of nanotubes should be considered as promising candidates for active elements of amplifiers and generators of coherent THz radiation.

We have also shown that an electric field, which is applied normally to the axis of long-period chiral nanotubes, significantly modifies their band structure near the edge of the Brillouin zone. This results in the negative effective-mass region at the energy scale below the high-energy phonon-emission threshold. This effect can be used for an efficient frequency multiplication in the THz range. Finally, we have discussed the feasibility of using the effect of the magnetic field, which opens energy gaps and allows optical transitions in armchair nanotubes, for creating tunable THz detectors and emitters.

Acknowledgments

References

Agarwal, G. S. (1975). Quantum electrodynamics in the presence of dielectrics and conductors. I. Electromagnetic-field response functions and black-body fluctuations in finite geometries. *Phys. Rev. A 11*, 230–242.

Akturk, A., N. Goldsman, and G. Pennington (2007a). Self-consistent ensemble Monte Carlo simulations show terahertz oscillations in single-walled carbon nanotubes. *J. Appl. Phys. 102*, 073720.

Akturk, A., N. Goldsman, and G. Pennington (2007b). Terahertz current oscillations in single-walled zigzag carbon nanotubes. *Phys. Rev. Lett. 98*, 166803.

Alekseev, K. N., M. V. Gorkunov, N. V. Demarina, T. Hyart, N. V. Alexeeva, and A. V. Shorokhov (2006). Suppressed absolute negative conductance and generation of high-frequency radiation in semiconductor superlattices. *Europhys. Lett. 73*, 934–940.

Ando, T., T. Nakanishi, and R. Saito (1997). Impurity scattering in carbon nanotubes—Absence of back scattering. *J. Phys. Soc. Jpn. 67*, 1704–1713.

Batrakov, K. G., P. P. Kuzhir, and S. A. Maksimenko (2006). Radiative instability of electron beam in carbon nanotubes. *Proc. SPIE 6328*, 63280Z.

Berestetskii, V. B., E. M. Lifshitz, and L. P. Pitaevskii (1997). *Quantum Electrodynamics*. Oxford, U.K.: Butterworth-Heinemann.

Bondarev, I. V., G. Y. Slepyan, and S. A. Maksimenko (2002). Spontaneous decay of excited atomic states near a carbon nanotube. *Phys. Rev. Lett. 89*, 115504.

Burke, P. J., S. Li, and Z. Yu (2006). Quantitative theory of nanowire and nanotube antenna performance. *IEEE Trans. Nanotechnol. 5*, 314–334.

Carminati, R. and J.-J. Greffet (1999). Near-field effects in spatial coherence of thermal sources. *Phys. Rev. Lett. 82*, 1660–1663.

Charlier, J.-C., X. Blase, and S. Roche (2007). Electronic and transport properties of nanotubes. *Rev. Mod. Phys. 70*, 677–732.

Colton, D. and R. Kress (1983). *Integral Equation Methods in Scattering Theory*. New York: Wiley.

Di Carlo, A., A. Pecchia, E. Petrolati, and C. Paoloni (2006). Modelling of carbon nanotube-based devices: From nanofets to THz emitters. *Proc. SPIE 6328*, 632808.

Dragoman, D. and M. Dragoman (2004a). Terahertz fields and applications. *Prog. Quantum Electron. 28*, 1–66.

Dragoman, D. and M. Dragoman (2004b). Terahertz oscillations in semiconducting carbon nanotube resonant-tunnelling diodes. *Physica E 24*, 282–289.

Dragoman, D. and M. Dragoman (2005). Terahertz continuous wave amplification in semiconductor carbon nanotubes. *Physica E 25*, 492–496.

Dragoman, M., A. Cismaru, H. Hartnagel, and R. Plana (2006). Reversible metal-semiconductor transitions for microwave switching applications. *Appl. Phys. Lett. 88*, 073503.

Dresselhaus, M. (2004). Nanotube antennas. *Nature (London) 432*, 959.

Dresselhaus, M. S., G. Dresselhaus, and P. Avouris (Eds.) (2000). *Carbon Nanotubes*. Berlin, Germany: Springer.

Florescu, M., K. Busch, and J. P. Dowling (2007). Thermal radiation in photonic crystals. *Phys. Rev. B 75*, 201101(R).

Freitag, M., V. Pereibenos, J. Chen et al. (2004). Hot carrier electroluminescence from a single carbon nanotube. *Nano Lett. 4*, 1063–1066.

Goupalov, S. V. (2005). Optical transitions in carbon nanotubes. *Phys. Rev. B 72*, 195403.

Grüneis, A., R. Saito, G. G. Samsonidze et al. (2003). Inhomogeneous optical absorption around the k point in graphite and carbon nanotubes. *Phys. Rev. B 67*, 165402.

Gunlycke, D., C. J. Lambert, S. W. D. Bailey, D. G. Pettifor, G. A. D. Briggs, and J. H. Jefferson (2006). Bandgap modulation of narrow-gap carbon nanotubes in a transverse electric field. *Europhys. Lett. 73*, 759–764.

Hanson, G. W. (2005). Fundamental transmitting properties of carbon nanotube antennas. *IEEE Trans. Antennas Propag. 53*, 3426–3435.

Henkel, C., K. Joulain, R. Carminati, and J.-J. Greffet (2000). Spatial coherence of thermal near-fields. *Opt. Commun. 186*, 57–67.

Jackson, J. D. (1999). *Classical Electrodynamics*. New York: Wiley.

Javey, A., J. Guo, M. Paulsson et al. (2004). High-field quasiballistic transport in short carbon nanotubes. *Phys. Rev. Lett. 92*, 106804.

Jiang, J., R. Saito, A. Gruneis, G. Dresselhaus, and M. S. Dresselhaus (2004). Optical absorption matrix elements in single-wall carbon nanotubes. *Carbon 42*, 3169–3176.

Joulain, K., R. Carminati, J.-P. Mulet, and J.-J. Greffet (2003). Definition and measurement of the local density of electromagnetic states close to an interface. *Phys. Rev. B 68*, 245405.

Joulain, K., J.-P. Mulet, F. Marquier, R. Carminati, and J.-J. Greffet (2005). Surface electromagnetic waves thermally excited: Radiative heat transfer, coherence properties and casimir forces revisited in the near field. *Surf. Sci. Rep. 57*, 59–112.

Kane, C. L. and E. J. Mele (1997). Size, shape, and low energy electronic structure of carbon nanotubes. *Phys. Rev. Lett. 78*, 1932–1935.

Kibis, O. V. and M. E. Portnoi (2005). Carbon nanotubes: A new type of emitter in the terahertz range. *Tech. Phys. Lett. 31*, 671–672.

Kibis, O. V. and M. E. Portnoi (2007). Semiconductor nanohelix in electric field: A superlattice of the new type. *Tech. Phys. Lett. 33*, 878–880.

Kibis, O. V. and M. E. Portnoi (2008). Superlattice properties of semiconductor nanohelices in a transverse electric field. *Physica E 40*, 1899–1901.

Kibis, O. V., S. V. Malevannyy, L. Hugget, D. G. W. Parfitt, and M. E. Portnoi (2005a). Superlattice properties of helical nanostructures in a transverse electric field. *Electromagnetics 25*, 425–435.

Kibis, O. V., D. G. W. Parfitt, and M. Portnoi (2005b). Superlattice properties of carbon nanotubes in a transverse electric field. *Phys. Rev. B 71*, 035411.

Kibis, O. V., M. R. da Costa, and M. E. Portnoi (2007). Generation of terahertz radiation by hot electrons in carbon nanotubes. *Nano Lett. 7*, 3414–3417.

Kibis, O. V., M. R. da Costa, and M. E. Portnoi (2008). Carbon nanotubes as a basis for novel terahertz devices. *Physica E 40*, 1766–1768.

Laroche, M., R. Carminati, and J.-J. Greffet (2006). Coherent thermal antenna using the photonic slab. *Phys. Rev. Lett. 96*, 123903.

Lee, M. and M. C. Wanke (2007). Searching for a solid-state terahertz technology. *Science 316*, 64–65.

Léonard, F. and J. Tersoff (2000). Negative differential resistance in nanotube devices. *Phys. Rev. Lett. 85*, 4767–4780.

Li, P., P. Li, K. Jiang, M. Liu, Q. Li, S. Fana, and J. Sun (2003). Polarized incandescent light emission from carbon nanotubes. *Appl. Phys. Lett. 82*, 1763–1765.

Li, Y., U. Ravaioli, and S. V. Rotkin (2006). Metal-semiconductor transition and fermi velocity renormalization in metallic carbon nanotubes. *Phys. Rev. B 73*, 034415.

Lifshitz, E. M. and L. P. Pitaevskii (1980). *Statistical Physics: Theory of the Condensed State*. Oxford, U.K.: Pergamon Press.

Lin, M. F. and D. S. Chuu (1998). Electronic states of toroidal carbon nanotubes. *J. Phys. Soc. Jpn. 67*, 259–263.

Lin, M. F. and W.-K. Shung (1993). Elementary excitations in cylindrical tubules. *Phys. Rev. B 47*, 6617–6624.

Lu, C., L. An, Q. Fu, J. Liu, H. Zhang, and J. Murduck (2006). Schottky diodes from asymmetric metal-nanotube contacts. *Appl. Phys. Lett. 88*, 133501.

Maksimenko, A. S. and G. Y. Slepyan (2000). Negative differential conductivity in carbon nanotubes. *Phys. Rev. Lett. 84*, 362–365.

Manohara, H. M., M. J. Bronikowski, M. Hoenk, B. D. Hunt, and P. H. Siegel (2005). High-current-density field emitters based on arrays of carbon nanotube bundles. *J. Vac. Sci. Technol. B 23*, 157–161.

Milošević, I., T. Vuković, S. Dmitrović, and M. Damnjanović (2003). Polarized optical absorption in carbon nanotubes: A symmetry-based approach. *Phys. Rev. B 67*, 165418.

Murakami, Y., S. M. E. Einarsson, and T. Edamura (2005). Polarization dependent optical absorption properties of single-walled carbon nanotubes and methodology for the evaluation of their morphology. *Carbon 43*, 2664–2667.

Nemilentsau, A. M., G. Y. Slepyan, and S. A. Maksimenko (2007). Thermal radiation from carbon nanotubes in the terahertz range. *Phys. Rev. Lett. 99*, 147403.

Novotny, L. and B. Hecht (2006). *Principles of Nano-Optics*. Cambridge, U.K.: Cambridge University Press.

Odintsov, A. A. (2000). Schottky barriers in carbon nanotube heterojunctions. *Phys. Rev. Lett. 85*, 150–153.

Ouyang, M., J.-L. Huang, C. L. Cheung, and C. M. Lieber (2001). Energy gaps in "metallic" single-walled carbon nanotubes. *Science 292*, 702–705.

Oyama, Y., R. Saito, K. Sato et al. (2006). Photoluminescence intensity of single-wall carbon nanotubes. *Carbon 44*, 873–879.

Park, J.-Y., S. Resenblatt, Y. Yaish et al. (2004). Electron-phonon scattering in metallic single-wall carbon nanotubes. *Nano Lett. 4*, 517–520.

Pennington, G. and N. Goldsman (2003). Semiclassical transport and phonon scattering of electrons in semiconducting carbon nanotubes. *Phys. Rev. B 68*, 045426.

Perebeinos, V., J. Tersoff, and P. Avouris (2005). Electron-phonon interaction and transport in semiconducting carbon nanotubes. *Phys. Rev. Lett. 94*, 086802.

Popov, V. N. and L. Henrard (2004). Comparative study of the optical properties of single-walled carbon nanotubes within orthogonal and nonorthogonal tight-binding models. *Phys. Rev. B 70*, 115407.

Portnoi, M. E., O. V. Kibis, and M. R. da Costa (2006). Terahertz emitters and detectors based on carbon nanotubes. *Proc. SPIE 6328*, 632805.

Portnoi, M. E., O. V. Kibis, and M. R. da Costa (2008). Terahertz applications of carbon nanotubes. *Superlattices Microstruct. 43*, 399–407.

Reich, S., C. Thomsen, and J. Maultzsch (2004). *Carbon Nanotubes: Basic Concepts and Physical Properties*. Berlin, Germany: Wiley.

Richter, M., S. Butscher, M. Schaarschmidt, and A. Knorr (2007). Model of thermal terahertz light emission from a two-dimensional electron gas. *Phys. Rev. B 75*, 115331.

Ruzicka, B., L. Degiorgi, R. Gaal, L. Thien-Nga, R. Bacsa, J.-P. Salvetat, and L. Forro (2000). Optical and dc conductivity study of potassium-doped single-walled carbon nanotube films. *Phys. Rev. B 61*, R2468–R2471.

Rytov, S. (1958). Correlation theory of thermal fluctuations in isotropic medium. *Sov. Phys. JETP 6*, 130–140.

Rytov, S., Y. Kravtsov, and V. Tatarskii (1989). *Principles of Statistical Radiophysics*, Volume 3. Berlin, Germany: Springer-Verlag.

Saito, R., G. Dresselhaus, and M. S. Dresselhaus (1998). *Physical Properties of Carbon Nanotubes*. London, U.K.: Imperial College Press.

Saito, R., A. Grüneis, G. G. Samsonidze et al. (2004). Optical absorption of graphite and single-wall carbon nanotube. *Appl. Phys. A 78*, 1099–1105.

Schegrov, A. V., K. Joulain, R. Carminati, and G. -G. Greffet (2000). Near-field spectral effects due to electromagnetic surface excitations. *Phys. Rev. Lett. 85*, 1548–1551.

Sfeir, M. Y., T. Beetz, F. Wang et al. (2006). Optical spectroscopy of individual single-walled carbon nanotube of defined chiral structure. *Science 312*, 554–556.

Slepyan, G. Y., S. A. Maksimenko, V. P. Kalosha, J. Herrmann, E. E. B. Campbell, and I. V. Hertel (1999). Highly efficient high-order harmonic generation by metallic carbon nanotubes. *Phys. Rev. A 60*, 777–780.

Slepyan, G. Y., S. A. Maksimenko, V. P. Kalosha, A. V. Gusakov, and J. Herrmann (2001). High-order harmonic generation by conduction electrons in carbon nanotubes ropes. *Phys. Rev. A 63*, 053808.

Slepyan, G. Y., M. Shuba, S. Maksimenko, and A. Lakhtakia (2006). Theory of optical scattering by achiral carbon nanotubes and their potential as optical nanoantennas. *Phys. Rev. B 73*, 195416.

Svizhenko, A. and M. P. Anantram (2005). Effect of scattering and contacts on current and electrostatics in carbon nanotubes. *Phys. Rev. B 72*, 085340.

Tasaki, S., K. Maekawa, and T. Yamabe (1998). π-Band contribution to the optical properties of carbon nanotubes: Effects of chirality. *Phys. Rev. B 57*, 9301–9318.

Ugawa, A., A. G. Rinzler, and D. B. Tanner (1999). Far-infrared gaps in single-wall carbon nanotubes. *Phys. Rev. B 60*, R11305–R110308.

Wallace, P. R. (1947). The band theory of graphite. *Phys. Rev. 71*, 622–634.

Yang, M. H., K. B. K. Teo, W. I. Milne, and D. G. Hasko (2005). Carbon nanotube schottky diode and directionally dependent field-effect transistor using asymmetrical contacts. *Appl. Phys. Lett. 87*, 253116.

Yao, Z., C. Kane, and C. Dekker (2000). High-field electrical transport in single-wall carbon nanotubes. *Phys. Rev. Lett. 84*, 2941–2944.

Zener, C. (1934). A theory of the optical breakdown of solid dielectrics. *Proc. R. Soc. (Lond.) 145*, 523–529.

Author Queries

[AQ1] Please check the phrase "range of definition" for sense in the sentence starting "The range.…"

[AQ2] Please specify the exact section number in the sentence starting "By analogy with the previous section.…"

[AQ3] Please check whether the edit made to the sentence starting "At equilibrium…" is ok.

[AQ4] Can "multi-walled SWNTs" be changed to "multi-walled CNTs" since "SW" stands for "single-walled?"

[AQ5] Please check if the edit made to the sentence starting "That is why…" is correct.

[AQ6] In Equation 5.39, "b" has been changed to "h". Please check.

[AQ7] Please check if the edit of the sentence starting "This work…" is ok.